Materials Science & Engineering A 816 (2021) 141275

Contents lists available at ScienceDirect

Materials Science & Engineering A

journal homepage: www.elsevier.com/locate/msea

Effect of helical rolling on the bainitic microstructure and impact toughness of the low-carbon microalloyed steel

L.S. Derevyagina [a,*], A.I. Gordienko [a], N.S. Surikova [a], M.N. Volochaev [b,c]

[a] Institute of Strength Physics and Materials Science of Siberian Branch Russian Academy of Sciences, 2/4, Pr. Akademicheskii, Tomsk, 634055, Russia
[b] Kirensky Institute of Physics of the Siberian Branch of the Russian Academy of Sciences (SB RAS), Akademgorodok 50, Bld. 38, Krasnoyarsk, 660036, Russia
[c] Reshetnev Siberian State University of Science and Technology, 31, Pr. Krasnoyarsk Worker, Krasnoyarsk, 660037, Russia

ARTICLE INFO

Keywords:
Low-carbon microalloyed steel
Helical rolling
Microstructure
Bainite
Martensite–austenite constituent
Impact toughness

ABSTRACT

Ferrite-bainite microstructures and impact toughness of the X65 low-carbon microalloyed steel were investigated after helical rolling at 1000, 920, 850, and 810 °C followed by continuous cooling in air. After helical rolling at 1000 °C, granular bainite with large areas of the massive-shape martensite-austenite constituent (d = 1.5 μm) and a high fraction of twinned martensite (d > 2.0 μm) were observed in the steel. This caused a decrease in impact energy at low test temperatures (for example, 70 J at –70°C). Lowering the helical rolling temperature contributed to a reduction of dimensions of both ferrite-bainite and martensite-austenite constituent areas, as well as the replacement of the latter by a slender type one and an improvement in fracture toughness at the low temperatures. The highest impact energy level (210 J at –70 °C) was achieved after helical rolling at 850 °C due to the formation of a homogeneous microstructure, which included dispersed ferrite grains, granular bainite and small fractions of the slender type martensite-austenite constituent (d = 0.1–0.7 μm). In this case, areas of twinned martensite were absent.

1. Introduction

Issues of improving the mechanical properties of low-carbon low-alloyed steels (X65 and X70 grades) are given great attention by many researchers. These steels are widely used for shipbuilding, in the heavy industry, as well as in the construction of oil and gas pipelines, including at the Arctic region. One of the key challenges of such studies is cold brittleness. For the steels with the bcc lattice, the ductile-to-brittle transition is caused by high both Peierls barrier and critical stresses required for movements of dislocations with decreasing test temperatures [1].

To reduce the ductile-brittle transition temperature (DBTT) of low-carbon steels, carbon reduction and complex microalloying are recommended [2–4], as well as application of various thermo-mechanical processing (TMP) procedures [5,6]. TMP enables to change the microstructure, phase composition and dispersion of microstructural elements [7–10]. The coarse-grained microstructure contributes to enhance of local stress concentrations at grain boundaries, a decrease in cleavage resistance and an increase in DBTT. On the contrary, both cleavage resistance and fracture toughness are improved in the case of fine-grained microstructure [11]. Large regions of second phases (pearlite, carbides) negatively affect resistance to brittle fracture at low test temperatures. Therefore, reducing their proportions and sizes is one of the tasks of applying TMP. After TMP, an increase in cooling rate contributes to the formation of intermediate (shear) transformation products such as bainite and martensite [12–15]. The use of interrupted cooling enables to control the type of the bainite microstructures (granular bainite (GB), lower and upper bainite, as well as acicular ferrite). However, in many cases, the manufacturing processes for rolled steel parts involve cooling them in air after rolling. Depending on the steel chemical composition and heating modes, the bainite microstructure (mainly GB) is formed even at low cooling rates [14]. It has been shown that the acicular ferrite (AF) microstructure provides a high impact energy level and a low DBTT [7–9]. The GB formation results in lower impact energy values due to larger both grains and areas of the martensite-austenite (M–A) constituent [13]. Despite this fact, some authors have noted that the GB microstructure provides higher levels of both upper shelf energy (USE) and DBTT, compared with those for lath bainite [10,16] and the typical ferrite-pearlite microstructure [14]. In this regard, it is necessary to consider the possibility of the GB formation upon post-deformation cooling in air, and also seeks to optimize the microstructure in order to obtain a sufficient level of impact toughness.

A number of authors have noted that impact toughness can be

* Corresponding author.
E-mail address: lsd@ispms.tsc.ru (L.S. Derevyagina).

https://doi.org/10.1016/j.msea.2021.141275
Received 20 October 2020; Received in revised form 8 April 2021; Accepted 10 April 2021
Available online 24 April 2021

List of abbreviations

DBTT	ductile-brittle transition temperature
TMP	thermo-mechanical processing
M–A	martensite-austenite constituent
F	ferrite
B	bainite
P	pearlite
GB	granular bainite
UB	upper bainite
LM	lath martensite
LenM	lenticular martensite
TM	twinned martensite
LPB	lower plate bainite
DUB	degenerated upper bainite
T	troostite

improved by the formation of a homogeneous microstructure [17], as well as refining the M–A constituent areas [16]. Li et al. have found [18] that an increase in sizes of prior austenite grains causes an enhance the M–A constituent areas and a decrease in impact toughness. At the same time, the authors of [19] have specified that the M–A constituent areas embrittle metal if their sizes exceed 2 μm. Heating of steel before rolling has a significant effect on the type of the formed bainite microstructure and the M–A constituent. It has been shown in Ref. [19] that heating to temperatures close to Ac_3 enables to obtain the minimum sizes of the M–A constituent and their remote location from each other, which contributes to a high impact toughness level. The authors of [20] have found that the fraction of the M–A constituent changes depending on the interval of intercritical heating temperatures. Its maximum fraction is formed in the temperature range of Ac_1+(15–50 °C) and decreases as the critical point Ac_3 is approached. Most authors [21,22] have concluded that a decrease in impact toughness is associated with an increase in the fraction of the massive-shape M–A constituent, which contains more carbon [15] and regions of twinned martensite (TM) [23,24], and is also harder than the slender type one.

Helical rolling is one of the understudied TMP procedures. It is used for piercing blanks into sleeves, small-scale production of seamless pipes of small diameters, obtaining hollow work-pieces for the manufacture of hydraulic cylinder housings, bushings, piston pins, drill lock couplings, etc. [25–27]. In contrast to conventional longitudinal rolling, a large proportion of the shear strain component is realized due to the rotational-translational movement of a workpiece in this case. As a result, the steel microstructure is refined more intensively and the quality of rolled products is enhanced. Thus, the possibility of a significant improvement in the mechanical properties of the X65 steel has been shown in Refs. [28,29]. This has caused interest in further detailed investigations of the microstructure features and their relationship with the impact toughness levels. In this regard, the purpose of this research has been to study the effect of different temperature conditions of helical rolling (HR) followed by continuous cooling in air on the formation of the bainite microstructure and impact toughness of the low-carbon microalloyed X65 steel.

2. Material and methods

The chemical composition of the studied X65 steel is presented in Table 1. Thermo-kinetic curves were drawn for the as-received hot-rolled steel using an 'STA 409 PC Luxx' synchronous thermal analyzer. Then, the phase transformation temperatures were determined on their basis, which were Ac_1 = 788 °C and Ac_3 = 892 °C upon heating, and were Ar_1 = 767 °C, Ar_3 = 814 °C, and Bs = 569 °C upon cooling.

Four microstructures were investigated after the HR using different modes (Table 2). In all cases, six HR passes were carried out followed by continuous cooling in air. A detailed description of the HR conditions was given in Ref. [29].

Microstructural studies were performed using a 'Zeiss Axiovert 25' optical microscope (OM) and 'Philips SEM 515' scanning electron microscope (SEM). To reveal grain boundaries, the sample cross-sections were etched in a 3% HNO_3 alcohol solution. A 'Quanta 200 3D' system with electron and focused ion beams, as well as a 'NORDLYS Oxford Instruments HKL Technology' attachment, were used for automatic electron backscatter diffraction (EBSD) analysis. To study the microstructures by EBSD analysis, electrolytic polishing was performed in a 25 ml CrO_3 + 210 ml H_3PO_4 solution at a voltage of 13 V and room temperature. During EBSD analysis, the scanning step was varied from 0.3 up to 0.5 μm. The total density of the grain boundaries was calculated as the ratio of their summarized lengths to the visible investigated area. The densities of both high-angle grain boundaries (HAGB) and low-angle grain boundaries (LAGB) were determined as the ratio of their lengths to the total length of all grain boundaries.

Fine structure studies were performed using 'CM-12' and 'HT-7700' (Hitachi) transmission electron microscopes (TEM). For the local microstructure investigations in the bainitic areas, an 'FIB2100' system with a focused ion beam (FIB) was used to cut out foils from the corresponded regions previously found through the optical image analysis (Fig. 1, a). Then, the samples were prepared using the FIB setup (Fig. 1b and c). The phase composition was analyzed by indexing electron diffraction patterns. Diffraction in the converging electron beam with a diameter of 100 nm (selected area diffraction pattern) was used for analysis of local areas and the determination of twin martensite. Average grain sizes were assessed using OM, SEM, TEM micrographs by the linear intercept method.

Impact bending tests of standard V-notched samples with dimensions of 10 × 10 × 55 mm were carried out using an INSTRON MPX 450 pendulum impact testing system in the temperature range T_{test} from +20 to –70 °C.

3. Results

3.1. Optical metallography, scanning electron microscopy and EBSD analysis

As the HR temperature had been reduced, a decrease in sizes of ferrite and pearlite grains, as well as lowering the proportion of pearlite areas were observed in the X65 steel microstructure (Table 3) [29]. After the HR using mode I, the steel microstructure was characterized by

Table 2
The HR temperature modes.

HR mode	HR beginning temperature, °C	HR finishing temperature, °C
I	1000, in the γ-region	γ-region
II	920, in the γ-region	near Ar_3 in the γ-region,
III	850, in the (γ+α)-region	(γ+α)-region
IV	810, in the low part of the (γ+α)-region	Near Ar_1

Table 1
The chemical composition of the X65 steel.

Element	C	Mn	V	Nb	Si	Ti	Cu	Al	P	S
Composition (wt, %)	0.13	1.6	0.05	0.04	0.4	0.05	0.3	0.03	0.013	0.01

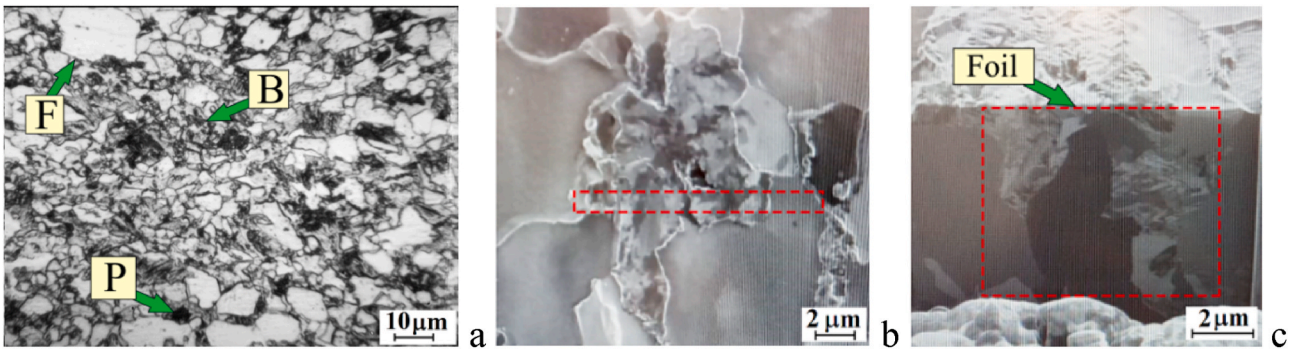

Fig. 1. An optical image of the steel microstructure after the HR using mode II (a, F is ferrite, B is bainite, P is pearlite) and SEM images showing the cross-section cutting process (b and c).

Table 3
Parameters of the X65 steel microstructure.

Sample	Grain sizes, μm	Pearlite volume fraction, %	Density of all grain boundaries, μm^{-1}	HAGB grain proportion, %	LAGB grain proportion, %
As-received	12.0	20.0	0.8	94.2	5.8
Mode I	5.4	14.5	1.1	86.5	13.5
Mode II	5.1	11.0	0.9	91.0	9.0
Mode III	3.3	8.5	1.8–2.0	85.0	15.0
Mode IV	3.2–3.6	5.0–8.0	1.8–2.4[a]	82.0–88.0[a]	12.0–18.0[a]

[a] Depending on the studied area on the rolled bar cross-sections (core or periphery).

uneven grain sizes (Fig. 2, a). Some of them reached 25 μm. After the HR using both modes II and III, the microstructures possessed more uniform grain sizes (Fig. 2b and c).

After lowering the HR temperature down to 810°C, different microstructures were observed in the core and peripheral areas on the rolled bar cross-sections. The microstructure was rather uniform in the peripheral areas (Fig. 2, d), but larger ferrite grains elongated in the rolling direction were found in the core ones (Fig. 2, e). The density of all grain boundaries and the LAGB proportion increased with decreasing the HR temperature (Table 3). In addition, bainitic areas were found (Fig. 3). Their proportions varied within 16–20% for different HR modes and in various cross-sections of the rolled bars. The microstructure in the bainitic areas was more dispersed in comparison with the ferrite matrix. After the HR using mode I, quasi-equiaxial GB grains were found in the steel microstructure. They were 2–4 μm in size and contained inclusions of more dispersed microstructural components, carbide particles, or the M–A constituent with dimensions up to 0.5–1.0 μm (Fig. 3, a). With a decrease in the HR temperature down to 920 °C, the bainite grains had a thin lath microstructure. However, it was not possible to determine the bainite type using the SEM images (Fig. 3, b). After the HR using both modes III and IV, dispersed bainite grains in the steel microstructure were characterized by quasi-equiaxial shapes typical of GB (Fig. 3c and d). The M–A constituent characterized by elongated shapes with thicknesses of 0.2–0.6 μm after the HR using mode IV. TEM investigations

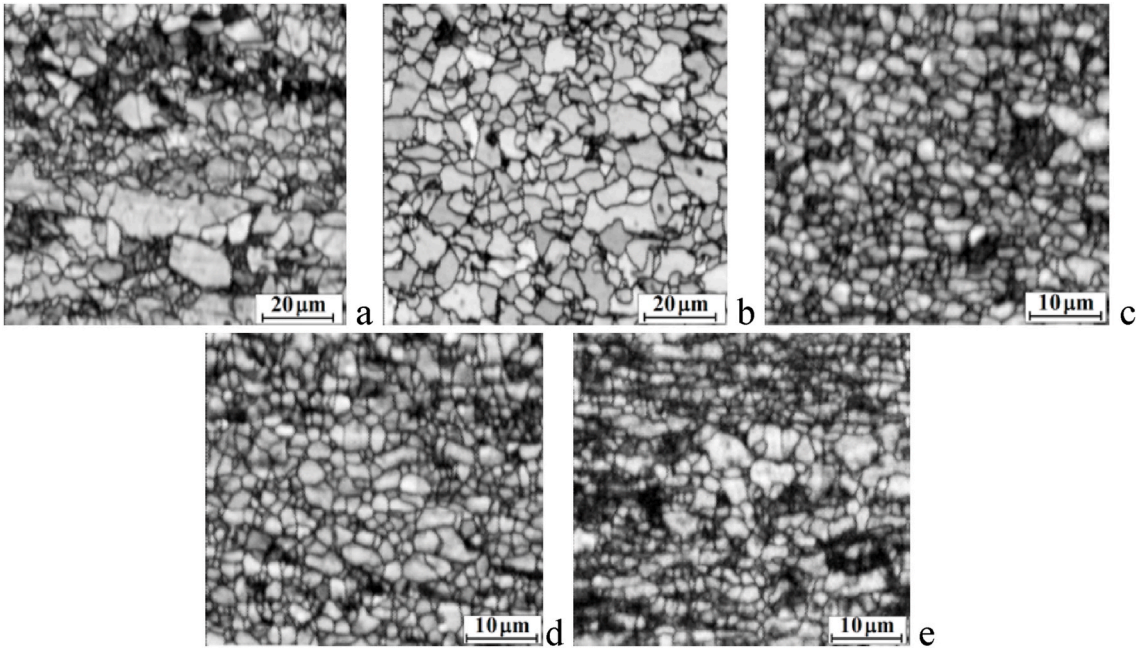

Fig. 2. The results of EBSD analysis for the steel after the HR using modes I (a), II (b), III (c), and IV (d–e): a–e – contrast maps; d– peripheral area; e – core area.

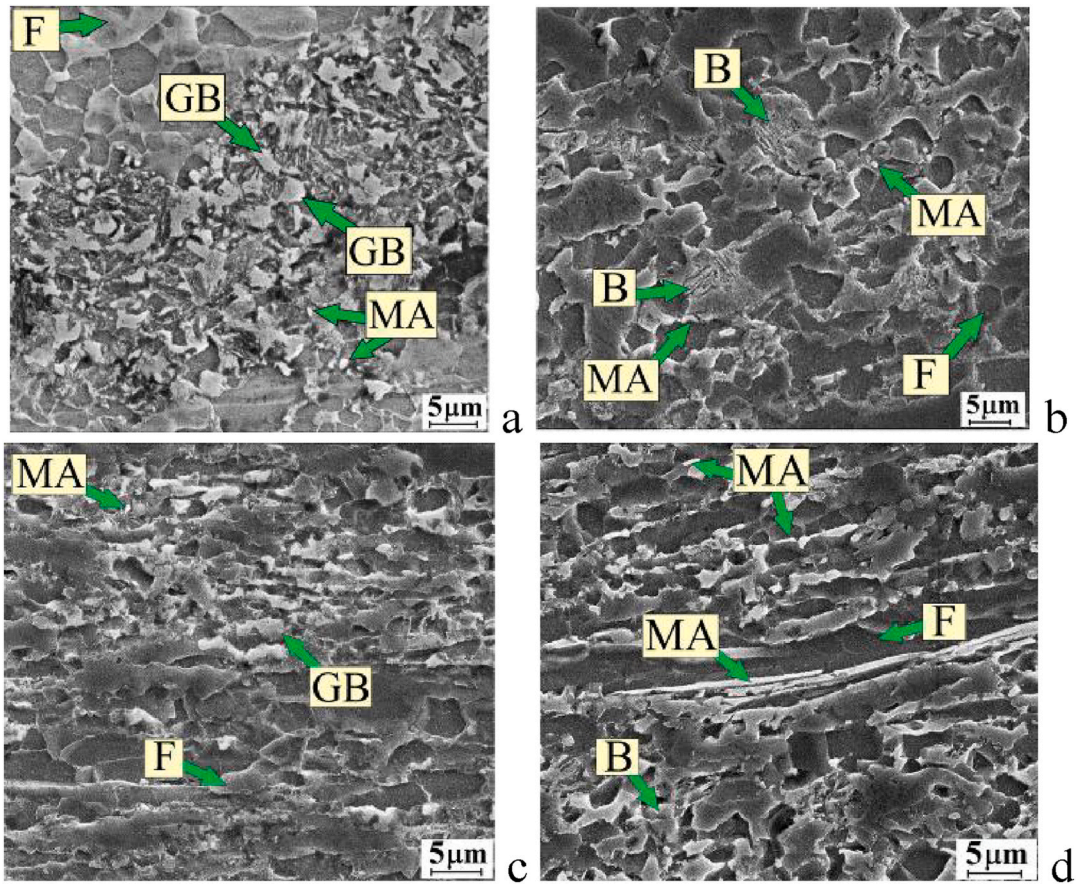

Fig. 3. The SEM-images of the steel microstructure after the HR using modes I (a), II (b), III (c), and IV (d).

were carried out for a more detailed study of the features for both the bainite microstructure and the M–A constituent in the steel after the HR using different modes.

3.2. Transmission electron microscopy

3.2.1. The HR using mode I

Quasi-polygonal ferrite grains (Fig. 4, a) and, at their boundaries, large particles of Fe_3C and Fe_2C carbides 50–180 nm in size as well as their small inclusions of 10–15 nm were observed in the X65 steel after the HR using mode I. Also, GB with grain sizes of 2–4 μm (Fig. 4, a) and a small fraction of lath bainite (170–450 nm wide) were found in the microstructure. In addition, 20–50 nm Fe_2C carbide inclusions (Fig. 4, b) were between the laths. This microstructure was typical for upper bainite (UB) [30].

Areas up to 1.0–1.5 μm in size with a more complex microstructure were found at the GB boundaries (Fig. 4, c). They consisted of lath martensite (LM) 70–150 nm wide, as well as areas of lenticular martensite (LenM) [31,32] with a midrib line divided the lenticular structure in the middle (Fig. 4, c). A weakly pronounced banded contrast was also found there, and microdiffraction patterns indicated the presence of TM inside (Fig. 4, e). Another TM area was in the center. At the boundaries of these microstructural conglomerates and between martensite laths, residual austenite precipitates were observed in thin interlayers 20–30 nm wide and larger patches with widths of 80–90 nm (Fig. 4, f). Since the R aspect ratio was less than four ($R = \frac{L_{max}}{L_{min}}$, where L_{max} and L_{min} were the maximum and minimum sizes of the M–A constituent, respectively [33]), this microstructural element could be attributed to the massive-shape M–A constituent.

Extensive TM areas consisted of parallel laths 5–10 nm wide were also found in the steel microstructure (Fig. 4, g). The dimensions of these areas varied in the range from 0.15 × 0.30 up to 1.6×2.2 μm. Microdiffraction patterns confirmed the presence of TM (Fig. 4, h). No residual austenite inclusions were observed near such areas.

3.2.2. The HR using mode II

After the HR using mode II, the steel microstructure included areas of upper lath bainite (UB; Fig. 5, a, d) and lower plate-like bainite (LPB; Fig. 5, d and f) in addition to ferrite. The widths of bainitic ferrite laths varied from 80 up to 400 nm Fe_2C carbide interlayers were found at the boundaries of UB laths (Fig. 5, b).

In other regions between the UB sublaths, there were layers of slender-shaped retained austenite 50–70 nm wide (Fig. 5, c). Their presence enabled to attribute this microstructure to degenerate upper bainite (DUB). LPB consisted of elliptical bainitic ferrite crystals with Fe_2C carbide precipitates (Fig. 5, e), which located inside grains at an angle to the axis of the α-crystal cross-section (Fig. 5, d and f). The sizes of the LPB areas were 2–3 μm, and the thicknesses of the carbide interlayers were 20–40 nm.

The M–A constituent areas of an elongated lenticular shape up to 0.3–2.5 μm were found along the LPB boundaries (Fig. 5, f). The fine microstructure was represented by highly dispersed TM inside (Fig. 5, f; microdiffraction pattern). Areas of retained austenite, predominantly in the form of thin interlayers with thicknesses of 30–120 nm, were identified along the M–A constituent boundaries (Fig. 5, g). Separate TM areas were observed only in local regions. Their dimensions did not exceed 150–300 nm (Fig. 5, h).

3.2.3. The HR using mode III

Ferrite grains were evenly interlaced with predominantly GB ones (1.5–2.5 μm in size) in the steel microstructure after the HR using mode III (Fig. 6a and b).

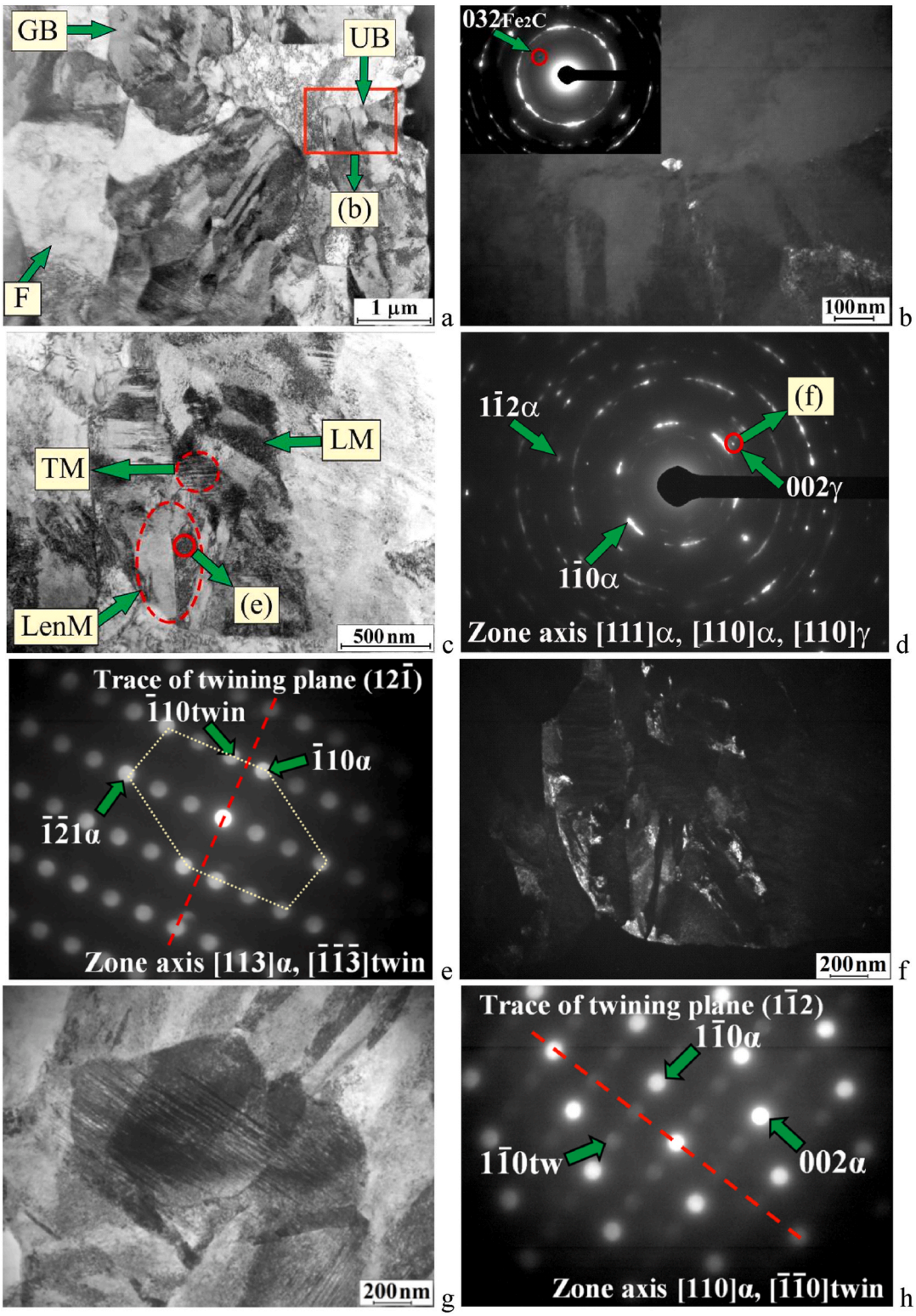

Fig. 4. TEM images of the steel microstructure after the HR using mode I: bright-field images (a, c, g); dark-field image in the 032 reflex from Fe_2C (b); microdiffraction pattern (d): reflexes of the [111]α, [110]α; [110]γ zones are indicated; microdiffraction pattern (e): reflexes of the [113]α, [$\bar{1}\bar{1}\bar{3}$]twin zones are indicated; dark-field image in the 002 reflex from γ-Fe (f); microdiffraction pattern (h): reflexes of the [110]α, [$\bar{1}\bar{1}$0]twin zones are indicated.

Reflexes from austenite were observed in the microdiffraction pattern (Fig. 6, c). However, the M–A constituent areas were difficult to find in the microstructure by TEM due to their small fraction and dispersion. In rare cases, the M–A constituent areas with sizes in the range of 0.2–0.7 μm were visible. The diffraction patterns from such areas revealed reflections of residual austenite and weak ones of the α-phase (Fig. 6, d), between which the [111]α//[011]γ Kurdyumov-Zags orientation relation was fulfilled.

A small fraction of LPB with dimensions of (1.0–1.3) × 2.2 μm and inclusions of Fe_2C carbide were also revealed in the microstructure

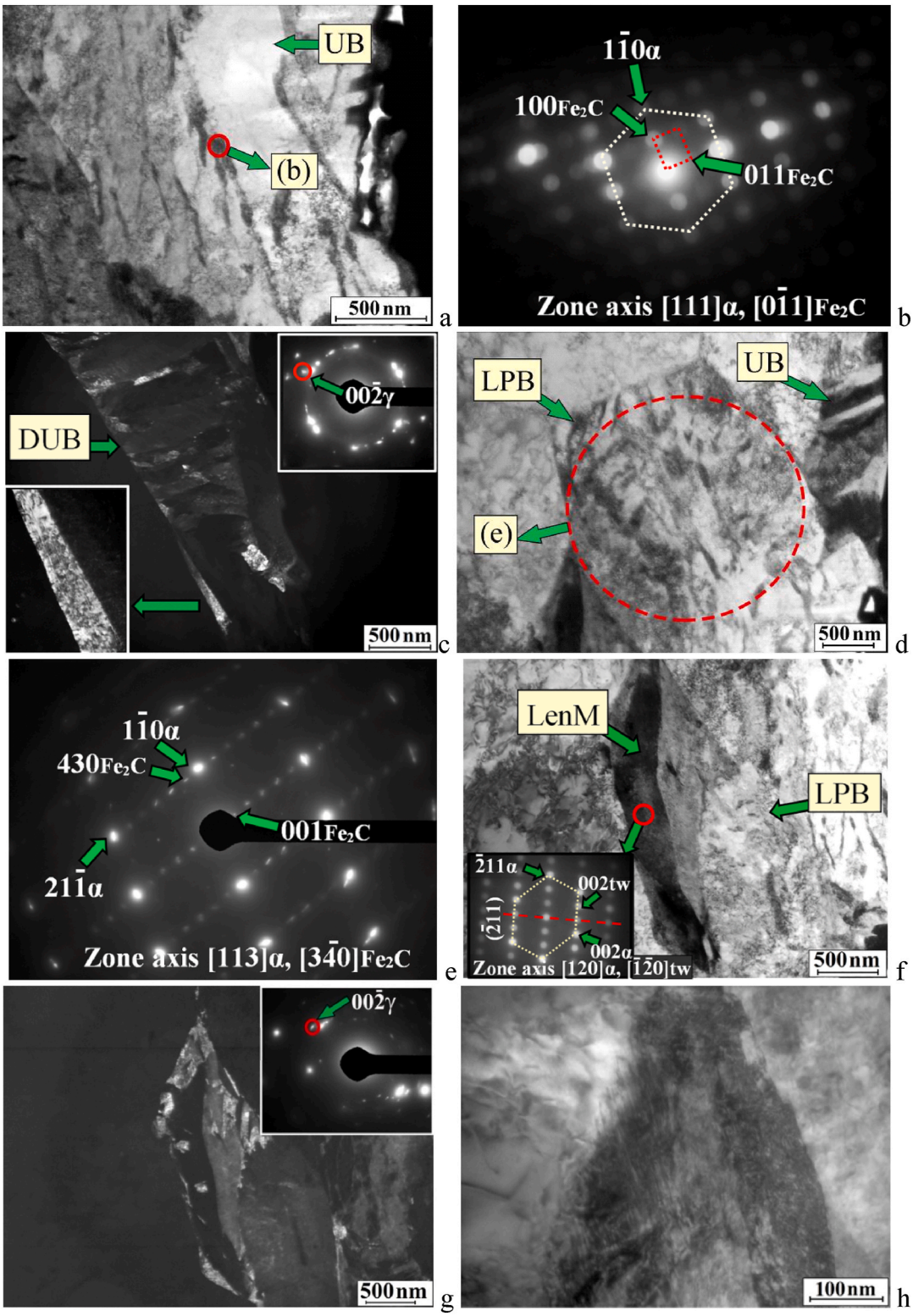

Fig. 5. TEM images of the steel microstructure after the HR using mode II: bright-field images (a, d, f, h); microdiffraction pattern (b): reflexes of the [111]α, [0$\bar{1}$1] Fe_2C zones are indicated; dark-field image in the 00$\bar{2}$ reflex from γ-Fe (c); microdiffraction pattern (e): reflexes of the [113]α, [3$\bar{4}$0]Fe_2C zones are indicated; dark-field image in the 00$\bar{2}$ reflex from γ-Fe (g).

(Fig. 6, e). In addition, interlayers and individual particles of Fe_3C carbide were observed at the boundaries of both ferrite and bainite grains (Fig. 6, f). No TM areas were found.

3.2.4. *The HR using mode IV*

Quasi-polygonal ferrite grains 1.0–3.0 μm in size (Fig. 7, a) and a small fraction of troostite (T) grains (400–600 nm) with ferrite lath 70–120 nm thick, as well as cementite laths with dimensions of 7–20 nm were in the steel microstructure after the HR using mode IV (Fig. 7, b).

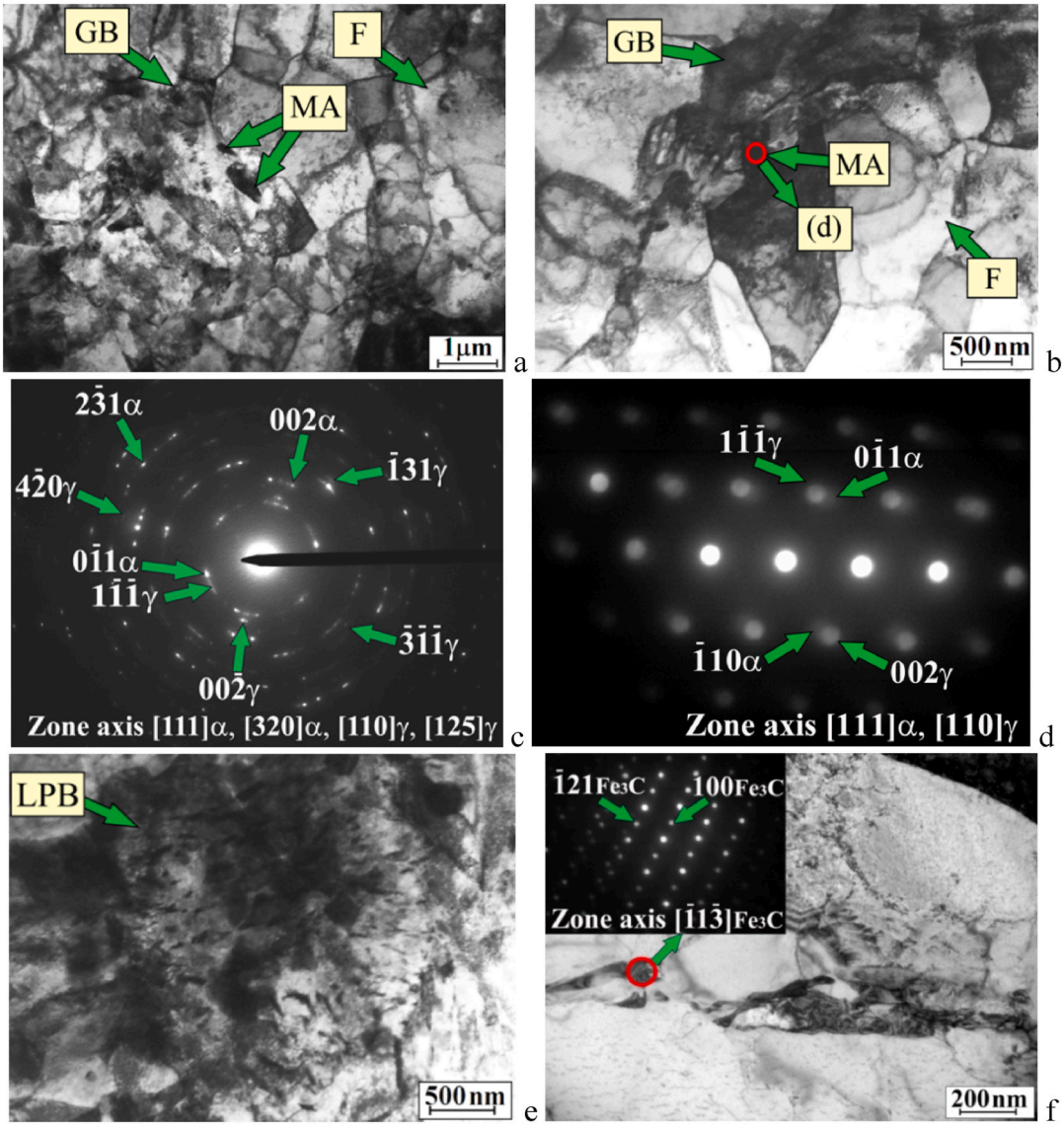

Fig. 6. TEM images of the steel microstructure after the HR using mode III: bright-field images (a, b, e); microdiffraction pattern (c): reflexes of the [111]α, [110]γ are indicated; microdiffraction pattern (d) of the region indicated in Fig. 5, b: reflexes of the [111]α, [110]γ zones are indicated; bright-field image and microdiffraction pattern (f): reflexes of the [$\bar{1}\bar{1}\bar{3}$] Fe_3C zones are indicated.

Its characteristic feature was the absence of pronounced bainite areas. Nevertheless, large aggregates were found that consisted of different microstructural components (Fig. 7c and d). One of such components with dimensions of 0.6–1.9 μm included UB laths 90–140 nm wide (Fig. 7, c), as well as both LenM and TM areas between them. Another example of an aggregate 0.8×1.9 μm in size with an even more complex microstructure is shown in Fig. 7, d.

The T region was distinguished inside, and the diffraction pattern of this area indicated the fulfillment of the [113]α ∥ [1$\bar{1}\bar{1}$]Fe_3C Yu. A. Bagaryatskiy orientational relation between ferrite and cementite lattices, which had realized during pearlite (bainitic) transformation. An area included laths with thicknesses of 50–80 nm was on the right side (shown in the top frame in Fig. 7, d). It could be attributed to both UB and martensite. In the microstructure of this conglomerate, there were TM regions with a typical microdiffraction pattern (Fig. 7, e): the trace of the twinning plane coincided with the direction of the twins. Areas were found at the boundaries of this conglomerate, the electron diffraction patterns of which indicated the presence of retained austenite and the α-phase (Fig. 7, f). The [111] α ∥ [011]γ Kurdyumov-Zags orientation relation was fulfilled between their lattices. Thus, these conglomerates could be attributed to the complex M–A constituent.

Regions up to 0.9×1.7 μm in size entirely composed of TM were also observed in the steel microstructure (Fig. 7g and h). Within them, weakly discernible long thin laths with a thickness of about 5 nm were visible (Fig. 7, g, enlarged in a frame).

3.3. Impact toughness tests

It was shown according to the results of impact bending tests that impact energy values of the hot-rolled X65 steel were 200, 24 and 10 J at temperatures of +20, –40 and –70 °C, respectively [29]. The HR processing improved impact toughness of the steel at the low test temperatures (Fig. 8). After the HR using mode III, the samples characterized by the highest impact energy value compared to the other ones. At the same time, the impact energy values did not reduce, remaining at a high level with a decrease in the test temperature down to –70 °C. After the HR using mode I, the impact energy level was the lowest of all samples tested at the low temperatures.

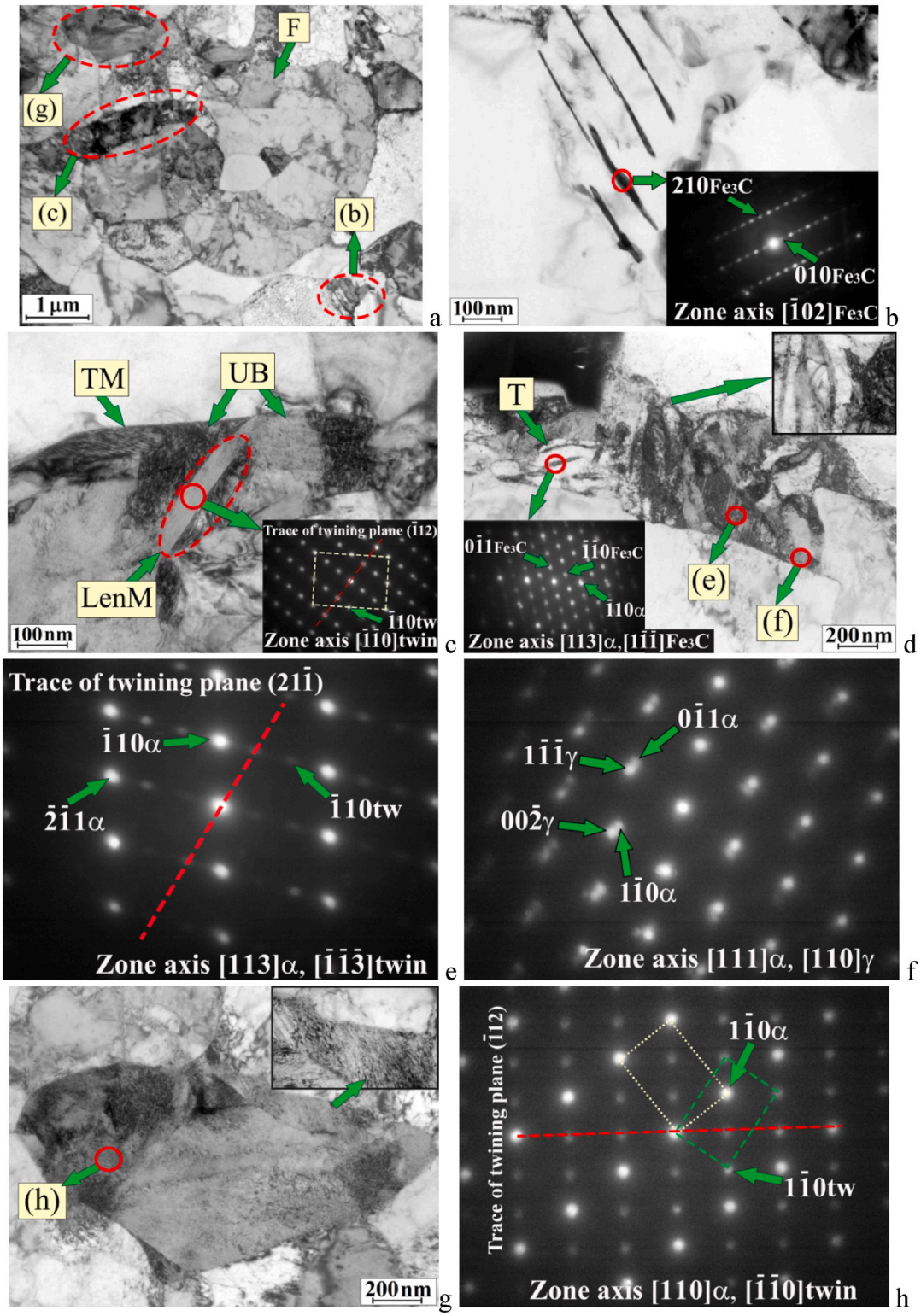

Fig. 7. TEM-images of the steel microstructure after the HR using mode IV: bright-field images (a–d, g); microdiffraction pattern (e) of the region indicated in Fig. 6, d: reflexes of the [113]α, [$\overline{113}$]α zones are indicated; microdiffraction pattern (f) of the region indicated in Fig. 6, d: reflexes of the [111]α, [110]γ zones are indicated; microdiffraction pattern (h): reflexes of the [110]α, [$\overline{110}$]twin zones are indicated.

4. Discussion

After the HR processing followed by continuous cooling in air, the complete diffusional decomposition of austenite into ferrite and pearlite did not occur in the X65 steel.

Bainitic transformation products were found in the microstructure. Their morphological patterns varied, but they were less distinct in comparison with steels cooled under isothermal conditions. This feature of the steel microstructures after continuously cooling was noted in Ref. [34].

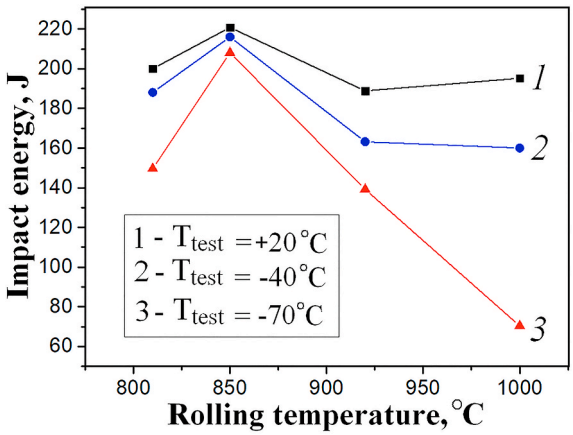

Fig. 8. Impact energy for the X65 steel vs the HR processing temperature.

The formation of ferrite in the upper part of the intercritical temperature range had resulted in the enrichment of austenite with carbon and an increase in its stability. These had caused the decrease in the critical quenching rate and the diffusionless decomposition of austenite into bainite/martensite. The variety of the bainitic transformation microstructures had determined the diffusional character of carbon redistribution in austenite and the precipitation of the second phases.

The amount of carbon dissolved in austenite had increased with rising the HR temperature. When it had reached 1130 °C, 1.7% of carbon had been in austenite, and it had been 0.8% at the Ac_1 point level. Therefore, austenite had contained more carbon when the steel had been heated up to 1000 °C upon the HR processing [35]. In addition, heat input had been higher, cooling rate had been lower, and the duration of carbon diffusion had been longer compared to those for other HR modes. These had contributed to the formation of GB and the massive-shape M–A constituent, which contained many large TM areas. As it was shown in Ref. [36], their presence was one of the reasons for the decrease in impact energy at the low temperatures. In Ref. [37], the formation of such complex massive regions of the M–A constituent was also found in the heat affected zone of the low-alloy steel. The authors noted that the formation of this type of the M–A constituent was the most critical for the steel fracture toughness. The sizes of austenite grains had affected the formation of the bainitic microstructure. At the high HR temperatures and the presence of large grains, the bainite-ferrite nucleation rate had been low, but its growth rate had been high [38]. Therefore, both granular and lath bainite grains, as well as the M–A constituent, were the largest compared to those for other HR modes (Table 4). These microstructural factors determined the lowest impact energy values at the test temperature of –70 °C (Fig. 8, Table 4). After the HR using mode I, the dimensions of the M–A constituent areas exceeded 2 μm, which were critical for fracture toughness in accordance with [19]. The refinement of grains and the M–A constituent areas was the main factor in reducing the DBBT. These results were consistent with the data obtained in Ref. [16].

When the temperature of the HR beginning decreased down to 920°C, deformation had finished in the Ar_3 region immediately before the ferrite transformation starting. A part of austenite had begun to enrich with carbon, reducing the bainite transformation points. Therefore, both UB and LPB (but not GB) had been formed. The change of the M–A constituent type to the slender one had happened as well. After the HR using mode II, its length reached 2.5 μm that reduced the M–A constituent proportion in the steel microstructure due to the elongated shapes. At the same time, TM areas were smaller. Consequently, the microstructure was characterized by the more uniform carbon distribution before the transformation compared to the steel after the HR using mode I. These changes contributed to the significant improvement in fracture toughness at the test temperature of –70 °C (Table 4). It was noted in Ref. [28] that positive factors in improving fracture toughness of the X65 steel was a more uniform alternation of microstructural components, the absence of uneven grain sizes, and a decrease in the proportion and dimensions of brittle pearlite inclusions.

The HR using mode III had finished at the temperature level of the existence of the (γ+α)-phases. The sizes of austenite grains, and, consequently, ferrite ones, were significantly lower compared to those after the HR using both modes I and II (Table 3). On the one hand, residual austenite was enriched in carbon and the bainitic transformation had to be shifted to the region of lower transformation temperatures. On the other hand, deformations, resulted in the presence of microstructural defects in the austenite, had increased the onset points [38,39] and the bainite transformation rate [38]. It was noted in Ref. [40] that fine austenite grains had reduced the ability of the steel to be quenched. Therefore, the GB formation had been stimulated. Initial austenite grains had been smaller before the transformation. Accordingly, the M–A constituent areas, which possessed shapes close to the slender type ones, were smaller as well (Table 4). A favorable factor was the absence of high-carbon TM regions. It was also shown in Ref. [41] that there were no TM areas in the fine-grained microstructure, while they were in the coarse-grained one. As a result, after the HR using mode III, the steel showed the highest impact energy levels over the entire test temperature range (Fig. 7).

The HR using mode IV had been carried out in the lower part of the (γ + α)-range and had finished near the Ac_1 critical point. Before cooling, a large proportion of dispersed ferrite grains had been formed in the steel microstructure. Residual austenite was significantly enriched with carbon and inhomogeneous in composition. It was shown in Ref. [42] that the region of the bainitic transformation had been absent, but the phase transformation points had been shifted to the martensitic transformation region upon cooling from temperatures close to the Ac_1 one. Therefore, there were very few obvious bainitic areas in the steel microstructure after the HR using mode IV. At the same time, small regions of dispersed UB laths 90–140 nm in size were located in the M–A constituent areas. It was difficult to distinguish them from martensite in some cases. A large proportion of the slender-type M–A constituent with the complex internal microstructure (Fig. 6c and d) as well as large areas of twinned martensite were found (Fig. 6, g). Consequently, it could be concluded that the increase in the amount of carbon in residual austenite before the phase transformations resulted in the complication of the M–A constituent microstructure (modes I and IV). For this reason, despite the dispersion of ferrite grains, the impact energy level was lower compared to that after the HR using mode III (Table IV). However, in spite of the high proportion and the sizes of the M–A constituent, the steel impact energy level was higher due to the dispersion of its microstructure compared to those after the HR using both modes I and II.

Table 4
Dimensions of the bainite elements and the impact energy values at the test temperature of –70 °C for the X65 steel after the HR using different temperature modes.

HR mode	Average bainitic ferrite dimensions, μm			M–A constituent (type and sizes, μm)	Twinned martensite areas (type and sizes, μm)	Impact energy at –70 °C, J
	GB	UB	LPB			
I	2–4	0.17–0.45	–	Massive, 1.0 × 1.5	Massive, 1.6 × 2.2	70
II	–	0.08–0.40	2–3	Slender, 0.3 × 2.5	Massive, 0.2 × 0.3	140
III	1.5–2.5	–	1.3–2.2	Slender, 0.1 × 0.7	–	210
IV		0.09–0.14		Slender, 0.8 × 1.9	Massive, 0.9 × 1.7	150

Thus, the correlation was observed between the impact energy level and the fractions/sizes of the M–A constituent and TM. The lower they were, the higher steel fracture toughness was. However, as noted by the authors of [43], it was important to understand when analyzing the microstructure that fracture toughness was determined not only by the most fragile component, but by the steel matrix as a complex substance. Despite the fact that many authors noted the negative effect of GB on fracture toughness, its high level was achieved due to the formation of a homogeneous microstructure, which included dispersed ferrite grains, granular bainite and small fractions of the slender type martensite-austenite constituent.

5. Conclusions

1. The HR processing of the X65 steel followed by subsequent continuous cooling in air resulted in the formation of the bainitic microstructure with the volume fraction of 16–20%. The variety of the HR temperature ranges caused different bainitic microstructures.
2. Granular bainite grains with the dimensions of 2–4.0 μm, upper bainite, as well as large areas of the massive-shape M–A constituent and the high proportion of twinned martensite with the sizes of more than 2 μm were observed in the steel microstructure after the HR processing from 1000 °C. These factors determined the low impact energy levels at the subzero temperatures.
3. After the HR temperature had been decreased down to 850 °C, the most dispersed ferrite-bainite microstructure was formed. The sizes of both granular bainite and M–A constituent areas, which transformed into the slender type, decreased. No areas of twinned martensite were observed. These factors contributed to the achievement of the maximum fracture toughness level of the steel at the subzero temperatures.
4. After the HR processing from 810 °C, the high proportion of large both M–A constituent and twinned martensite areas were found despite the microstructure dispersion. Therefore, a high level of fracture toughness could not be achieved.

Data availability

The raw/processed data required to reproduce these findings cannot be shared at this time as the data also forms part of an ongoing study.

CRediT authorship contribution statement

L.S. Derevyagina: Conceptualization, Methodology, Writing – original draft. **A.I. Gordienko:** Investigation, Visualization, Writing – review & editing. **N.S. Surikova:** Investigation, Visualization. **M.N. Volochaev:** Investigation.

Declaration of competing interest

The authors declare that they have no known competing financial interests or personal relationships that could have appeared to influence the work reported in this paper.

Acknowledgments

The work was performed according to the Government research assignment for ISPMS SB RAS.

TEM studies were carried out in Center of Federal Research Center of Kirensky Institute of Physics SB RAS. SEM studies was carried out in NANOTECH Centre of Institute of Strength Physics and Materials Science SB RAS.

The authors are grateful to Ivan Mishin for assistance in helical rolling of the steel, Ilya Vlasov for the impact bending test, and Mikhail Slobodyan for translation into English.

References

[1] V.M. Chernov, B.K. Kardashev, K.A. Moroz, Cold brittleness and fracture of metals with various crystal lattices: dislocation mechanisms, Tech. Phys. 61 (2016) 1015–1022, https://doi.org/10.1134/S1063784216070070.
[2] S.C. Liu, V.S.A Challa, V.V. Natarajan, R.D.K. Misra, D.M. Sidorenko, M. D. Mulholland, M. Manohar, J.E. Hartmann, Significant influence of carbon and niobium on the precipitation behavior and microstructural evolution and their consequent impact on mechanical properties in microalloyed steels, Mater. Sci. Eng., A 683 (2017) 70–82, https://doi.org/10.1016/j.msea.2016.11.102.
[3] G. Shi, H. Zhao, S. Zhang, Q. Wang, F. Zhang, Microstructural characteristics and impact fracture behaviors of low-carbon vanadium-microalloyed steel with different nitrogen contents, Mater. Sci. Eng., A 769 (2020) 138501, https://doi.org/10.1016/j.msea.2019.138501.
[4] L. Lan, Z. Chang, X. Kong, C. Qiu, D. Zhao, Phase transformation, microstructure, and mechanical properties of X100 pipeline steels based on TMCP and HTP concepts, J. Mater. Sci. 52 (2017) 1661–1678, https://doi.org/10.1007/s10853-016-0459-6.
[5] B. Hwang, C.G. Lee, S.J. Kim, Low-temperature toughening mechanism in thermomechanically processed high-strength low-alloy steels, Metall. Mater. Trans. A Phys. Metall. Mater. Sci. 42 (2011) 717–728, https://doi.org/10.1007/s11661-010-0448-3.
[6] X.L. Yang, X.D. Tan, Y.B. Xu, Z.P. Hu, Y.M. Yu, D. Wu, Effect of rolling process on impact toughness in high strength low carbon bainitic steel, in: Mater. Sci. Forum, Trans Tech Publications Ltd, 2015, pp. 743–749. https://doi.org/10.4028/www.scientific.net/MSF.816.743.
[7] S. Ghosh, S. Mula, Thermomechanical processing of low carbon Nb-Ti stabilized microalloyed steel: microstructure and mechanical properties, Mater. Sci. Eng., A 646 (2015) 218–233, https://doi.org/10.1016/j.msea.2015.08.072.
[8] M.C. Zhao, K. Yang, Y. Shan, The effects of thermo-mechanical control process on microstructures and mechanical properties of a commercial pipeline steel, Mater. Sci. Eng., A 335 (2002) 14–20, https://doi.org/10.1016/S0921-5093(01)01904-9.
[9] H.F. Lan, L.X. Du, R.D.K. Misra, Effect of microstructural constituents on strength-toughness combination in a low carbon bainitic steel, Mater. Sci. Eng., A 611 (2014) 194–200, https://doi.org/10.1016/j.msea.2014.05.084.
[10] B. Hwang, C.G. Lee, T.H. Lee, Correlation of microstructure and mechanical properties of thermomechanically processed low-carbon steels containing boron and copper, Metall. Mater. Trans. A Phys. Metall. Mater. Sci. 41 (2010) 85–96, https://doi.org/10.1007/s11661-009-0070-4.
[11] L.L. Feng, F. Hu, W.W. Qiao, X.Y. Lu, Microstructure and properties of 09MnNiDR steel for -70 °C ultra low temperature environment, Kang T'ieh/Iron Steel 55 (2020) 89–95, https://doi.org/10.13228/j.boyuan.issn0449-749x.20190565.
[12] V.V. Natarajan, S. Liu, V.S.A. Challa, R.D.K. Misra, D.M. Sidorenko, M. D. Mulholland, M. Manohar, J.E. Hartmann, Processing-structure-mechanical property relationship in Ti-Nb microalloyed steel: continuous cooling versus interrupted cooling, Mater. Sci. Eng., A 671 (2016) 254–263, https://doi.org/10.1016/j.msea.2016.06.061.
[13] M. Ali, D. Porter, J. Kömi, M. Eissa, H. El Faramawy, T. Mattar, Effect of cooling rate and composition on microstructure and mechanical properties of ultrahigh-strength steels, J. Iron Steel Res. Int. 26 (2019) 1350–1365, https://doi.org/10.1007/s42243-019-00276-0.
[14] S. jun Jia, B. Li, Q. you Liu, Y. Ren, S. Zhang, H. Gao, Effects of continuous cooling rate on morphology of granular bainite in pipeline steels, J. Iron Steel Res. Int. 27 (2020) 681–690, https://doi.org/10.1007/s42243-019-00346-3.
[15] J. Chen, S. Tang, Z.Y. Liu, G.D. Wang, Microstructural characteristics with various cooling paths and the mechanism of embrittlement and toughening in low-carbon high performance bridge steel, Mater. Sci. Eng., A 559 (2013) 241–249, https://doi.org/10.1016/j.msea.2012.08.091.
[16] T. Jia, Y. Zhou, X. Jia, Z. Wang, Effects of microstructure on CVN impact toughness in thermomechanically processed high strength microalloyed steel, Metall. Mater. Trans. A Phys. Metall. Mater. Sci. 48 (2017) 685–696, https://doi.org/10.1007/s11661-016-3893-9.
[17] N. Kang, Y. Lee, S. Byun, K. Kim, K. Kim, J. Chung, K. Cho, Quantitative analysis of microstructural and mechanical behavior for Fe-0.1C-(V, Nb) steels as a function of the final rolling temperature, Mater. Sci. Eng., A 499 (2009) 157–161, https://doi.org/10.1016/j.msea.2007.11.145.
[18] X. Li, X. Ma, S.V. Subramanian, C. Shang, R.D.K. Misra, Influence of prior austenite grain size on martensite-austenite constituent and toughness in the heat affected zone of 700MPa high strength linepipe steel, Mater. Sci. Eng., A 616 (2014) 141–147, https://doi.org/10.1016/j.msea.2014.07.100.
[19] X. Li, Y. Fan, X. Ma, S.V. Subramanian, C. Shang, Influence of Martensite-Austenite constituents formed at different intercritical temperatures on toughness, Mater. Des. 67 (2015) 457–463, https://doi.org/10.1016/j.matdes.2014.10.028.
[20] E. Bayraktar, D. Kaplan, Mechanical and metallurgical investigation of martensite-austenite constituents in simulated welding conditions, J. Mater. Process. Technol. 153–154 (2004) 87–92, https://doi.org/10.1016/j.jmatprotec.2004.04.021.
[21] N. Huda, A.R.H. Midawi, J. Gianetto, R. Lazor, A.P. Gerlich, Influence of martensite-austenite (MA) on impact toughness of X80 line pipe steels, Mater. Sci. Eng., A 662 (2016) 481–491, https://doi.org/10.1016/j.msea.2016.03.095.
[22] X.J. Di, L. Cai, X.X. Xing, C.X. Chen, Z.K. Xue, Microstructure and mechanical properties of intercritical heat-affected zone of X80 pipeline steel in simulated in-service welding, Acta Metall. Sin. (English Lett. 28 (2015) 883–891, https://doi.org/10.1007/s40195-015-0272-2.
[23] X. Li, C. Shang, X. Ma, B. Gault, S.V. Subramanian, J. Sun, R.D.K. Misra, Elemental distribution in the martensite–austenite constituent in intercritically reheated

coarse-grained heat-affected zone of a high-strength pipeline steel, Scripta Mater. 139 (2017) 67–70, https://doi.org/10.1016/j.scriptamat.2017.06.017.
[24] H. Okada, K. Ikeuchi, I. Hrivnak, Z. Li, Metallographic investigation of M-A constituent Deterioration and improvement of HAZ toughness in 780 and 980 MPa class HSLA steels welded with high heat inputs (2nd report), Weld. Int. 8 (1994) 886–892, https://doi.org/10.1080/09507119409548716.
[25] B.A. Romantsev, Y.V. Gamin, A.V. Goncharuk, A.S. Aleshchenko, Innovative equipment for producing cost-effective hollow billets for mechanical-engineering parts of small diameter, Metallurgist 61 (2017) 217–222, https://doi.org/10.1007/s11015-017-0480-2.
[26] S.P. Galkin, B.A. Romantsev, E.A. Kharitonov, Putting into practice innovative potential in the universal radial-shear rolling process, CIS Iron Steel Rev. (2014) 35–39, 2014.
[27] V.P. Romanenko, A.V. Fomin, V.V. Begnarskii, A.A. Yandimirov, A.N. Nikulin, Deformation action of screw rolling on a cast wheel billet, Metallurgist 56 (2013) 753–759, https://doi.org/10.1007/s11015-013-9653-9.
[28] L.S. Derevyagina, A.I. Gordienko, Y.I. Pochivalov, A.S. Smirnova, Modification of the structure of low-carbon pipe steel by helical rolling, and the increase in its strength and cold resistance, Phys. Met. Metallogr. 119 (2018) 83–91, https://doi.org/10.1134/S0031918X18010076.
[29] V.E. Panin, L.S. Derevyagina, S.V. Panin, A.R. Shugurov, A.I. Gordienko, The role of nanoscale strain-induced defects in the sharp increase of low-temperature toughness in low-carbon and low-alloy steels, Mater. Sci. Eng., A 768 (2019) 138491, https://doi.org/10.1016/j.msea.2019.138491.
[30] S. Zajac, V. Schwinnand, K.H. Tacke, Characterisation and quantification of complex bainitic microstructures in high and ultra-high strength linepipe steels, Mater. Sci. Forum 500–501 (2005) 387–394. https://doi.org/10.4028/www.scientific.net/msf.500-501.387.
[31] C. Wang, X. Wu, J. Liu, N. Xu, Transmission electron microscopy of martensite/austenite islands in pipeline steel X70, Mater. Sci. Eng., A 438–440 (2006) 267–271, https://doi.org/10.1016/j.msea.2006.02.118.
[32] H.Y. Lee, H.W. Yen, H.T. Chang, J.R. Yang, Substructures of martensite in Fe-1C-17Cr stainless steel, Scripta Mater. 62 (2010) 670–673, https://doi.org/10.1016/j.scriptamat.2010.01.022.
[33] E. Bonnevie, G. Ferrière, A. Ikhlef, D. Kaplan, J.M. Orain, Morphological aspects of martensite-austenite constituents in intercritical and coarse grain heat affected zones of structural steels, Mater. Sci. Eng., A 385 (2004) 352–358, https://doi.org/10.1016/j.msea.2004.06.033.
[34] G. Thewlis, Materials perspective: classification and quantification of microstructures in steels, Mater. Sci. Technol. 20 (2004) 143–160, https://doi.org/10.1179/026708304225010325.
[35] S. Endo, Effect of applied thermal cycle conditions on chemistry and volume fraction of M-A constituent formed in a low alloy steel, Tetsu-To-Hagane/Journal Iron Steel Inst. Japan. 84 (1998) 297–302, https://doi.org/10.2355/tetsutohagane1955.84.4_297.
[36] O.M. Akselsen, Grong, J.K. Solberg, Structure-property relationships in intercritical heat affected zone of low-carbon microalloyed steels, Mater. Sci. Technol. (United Kingdom). 3 (1987) 649–655, https://doi.org/10.1179/mst.1987.3.8.649.
[37] D.C. Ramachandran, S.D. Kim, J. Moon, C.H. Lee, J.H. Chung, E. Biro, Y. Do Park, Classification of martensite-austenite constituents according to its internal morphology in high-strength low alloy steel, Mater. Lett. 278 (2020) 128422, https://doi.org/10.1016/j.matlet.2020.128422.
[38] X. Liang, A.J. Deardo, A study of the influence of thermomechanical controlled processing on the microstructure of bainite in high strength plate steel, Metall. Mater. Trans. A Phys. Metall. Mater. Sci. 45 (2014) 5173–5184, https://doi.org/10.1007/s11661-014-2444-5.
[39] L. Lan, C. Qiu, D. Zhao, X. Gao, L. Du, Effect of reheat temperature on continuous cooling bainite transformation behavior in low carbon microalloyed steel, J. Mater. Sci. 48 (2013) 4356–4364, https://doi.org/10.1007/s10853-013-7251-7.
[40] P. Kirkwood, Enhancing the weldability of C-Mn pressure vessel steels — a tale of two elements, Energy Mater. (2014) 61–70, https://doi.org/10.1007/978-3-319-48765-6_7.
[41] K. Poorhaydari, B.M. Patchett, D.G. Ivey, Transformation twins in the weld HAZ of a low-carbon high-strength microalloyed steel, Mater. Sci. Eng., A 435–436 (2006) 371–382, https://doi.org/10.1016/j.msea.2006.07.055.
[42] Z. Li, X. Zhao, D. Shan, Impact toughness of subzones in the intercritical heat-affected zone of low-carbon bainitic steel, Materials (Basel) 11 (2018), https://doi.org/10.3390/ma11060959.
[43] J.B. Ju, W. sik Kim, J. il Jang, Variations in DBTT and CTOD within weld heat-affected zone of API X65 pipeline steel, Mater. Sci. Eng., A 546 (2012) 258–262, https://doi.org/10.1016/j.msea.2012.03.062.